JCB Journal of Cell Biology

ARTICLE

SPATA7 maintains a novel photoreceptor-specific zone in the distal connecting cilium

Rachayata Dharmat[1,2], Aiden Eblimit[2], Michael A. Robichaux[3], Zhixian Zhang[3], Thanh-Minh T. Nguyen[4,5], Sung Yun Jung[3], Feng He[3], Antrix Jain[3], Yumei Li[2], Jun Qin[3], Paul Overbeek[1], Ronald Roepman[4,5], Graeme Mardon[1,6], Theodore G. Wensel[3], and Rui Chen[1,2,3]

Photoreceptor-specific ciliopathies often affect a structure that is considered functionally homologous to the ciliary transition zone (TZ) called the connecting cilium (CC). However, it is unclear how mutations in certain ciliary genes disrupt the photoreceptor CC without impacting the primary cilia systemically. By applying stochastic optical reconstruction microscopy technology in different genetic models, we show that the CC can be partitioned into two regions: the proximal CC (PCC), which is homologous to the TZ of primary cilia, and the distal CC (DCC), a photoreceptor-specific extension of the ciliary TZ. This specialized distal zone of the CC in photoreceptors is maintained by SPATA7, which interacts with other photoreceptor-specific ciliary proteins such as RPGR and RPGRIP1. The absence of *Spata7* results in the mislocalization of DCC proteins without affecting the PCC protein complexes. This collapse results in destabilization of the axonemal microtubules, which consequently results in photoreceptor degeneration. These data provide a novel mechanism to explain how genetic disruption of ubiquitously present ciliary proteins exerts tissue-specific ciliopathy phenotypes.

Introduction

Primary cilia are organelles protruding from the cell surface that play key roles in sensory modalities such as photosensation, mechanosensation, and chemosensation across multiple different cell types and species (Gerdes et al., 2009; Drummond, 2012). Irrespective of the cell type, the primary cilium is comprised of three structural–functional modules: the basal body, the transition zone (TZ), and a microtubule-based axoneme. As a consequence of widespread distribution and diverse functions of primary cilia, mutations affecting the core protein components of these ciliary modules result in a diverse set of multisystemic, developmental, and degenerative disorders collectively called ciliopathies (Reiter and Leroux, 2017). However, a subset of ciliary genes encoding proteins housed in the TZ module, when muated, specifically display nonsyndromic defects in the retina such as Leber congenital amaurosis (Mendelian Inheritance in Man [MIM] ID 204000; Wang et al., 2009) and retinitis pigmentosa (RP; MIM ID 300029; Hong et al., 2001). To understand the mechanism of nonsyndromic ciliopathies, we investigated the photoreceptor connecting cilium (CC), a putative structural and functional homologue of the TZ in primary cilia.

The TZ is the proximal-most region of the ciliary axoneme that functions to compartmentalize the ciliary proteome. The TZ houses evolutionarily conserved protein complexes such as the Meckel syndrome (MKS; MIM ID 249000) complex (TCTN1, TCTN2, TMEM231, TMEM67, MKS1, MKS6, B9D1, B9D2, and AHI1) and the nephronophthisis syndrome (NPHP; MIM ID 256100) complex (NPHP1, NPHP4, and RPGRIP1L [RP GTPase regulator (RPGR)-interacting protein 1 (RPGRIP1)-like protein]). Members of these complexes interact among themselves and enable associations between the axoneme and the ciliary membrane, thereby maintaining the ciliary gate/barrier that regulates both ciliogenesis and protein trafficking within the cilium (Williams et al., 2011; Jensen et al., 2015; Li et al., 2016). Given the functional significance of the TZ in maintaining the ciliary composition, mutations in TZ genes often disrupt cilium stability, resulting in severe syndromic ciliopathy phenotypes (Reiter and Leroux, 2017). Interestingly, mutations in three TZ module genes, spermatogenesis-associated protein 7 (*SPATA7*), *RPGRIP1*, and *RPGR*, affect exclusively the photoreceptor sensory cilium. Although the precise interactions among members of the RPGR complex are not fully characterized, RPGR directly interacts with RPGRIP1, which interacts with SPATA7, NPHP4, and other ciliary proteins to form a complex (Roepman et al., 2000; Hong et al., 2001; Murga-Zamalloa et al., 2010). This RPGR complex

[1]Molecular and Human Genetics, Baylor College of Medicine, Houston, TX; [2]Human Genome Sequencing Center, Baylor College of Medicine, Houston, TX; [3]Verna and Marrs McLean Department of Biochemistry and Molecular Biology, Baylor College of Medicine, Houston, TX; [4]Department of Human Genetics, Radboud University Medical Center, Nijmegen, Netherlands; [5]Radboud Institute for Molecular Life Sciences, Radboud University Medical Center, Nijmegen, Netherlands; [6]Pathology and Immunology, Baylor College of Medicine, Houston, TX.

Correspondence to Rui Chen: ruichen@bcm.edu; A. Eblimit's present address is Dept. of Biomedical Engineering, University of Houston, Houston, TX.

is hypothesized to play a role in maintaining the structure and/or mediating protein transport in photoreceptor cells (Murga-Zamalloa et al., 2010; Remans et al., 2014). RPGR complex members are also present at the primary cilium TZ (Shu et al., 2005; Eblimit et al., 2015), where they interact with RPGRIP1L/MKS5 and CEP290, multifunctional proteins that are crucial for the stability of both MKS and NPHP complexes (Chang et al., 2006; Khanna et al., 2009; Li et al., 2016). Despite their localization at the TZ of the primary cilium, it is not understood how the loss of *SPATA7*, *RPGRIP1*, and *RPGR* specifically causes nonsyndromic retinal ciliopathies in both patients and mouse models lacking syndromic presentations (Meindl et al., 1996; Dryja et al., 2001; Wang et al., 2009).

The photoreceptor cells contain a highly specialized form of primary cilium called the photoreceptor sensory cilium (Gilliam et al., 2012). Similar to the primary cilium, the photoreceptor sensory cilium also comprises the proximal-most basal body, a TZ-like structural intermediate called the CC, as well as a specialized extension called the outer segment housed on an axoneme-like backbone. Classically, the photoreceptor CC is considered homologous to the primary cilium TZ; however, there are some key distinctions. For example, although known TZ protein complexes such as MKS and NPHP as well as other TZ proteins including CEP290 are essential in both structures (Craige et al., 2010; Patil et al., 2012; Cevik et al., 2013), a specialized set of ciliary proteins such as SPATA7, RPGR, and RPGRIP1 are functionally critical only for the CC (Hong et al., 2000; Rachel et al., 2012; Eblimit et al., 2015). Structurally, both the TZ and CC are marked by proteinaceous membrane connections including transition fibers (associated with the basal body), distal appendages (associated only with the base of the TZ), and the Y-links (connecting the TZ microtubule cylinder to ciliary membrane). However, the photoreceptor CC (1.5 µm in mice) extends approximately three times the length of the TZ (200–500 nm) found in other cells, suggesting that the CC is structurally more elaborate (Gilliam et al., 2012; Wensel et al., 2016; May-Simera et al., 2017). The strikingly unique feature of the CC is the presence of the outer segment at its distal end, a large complex membranous structure whose molecular composition is to a large extent unique to photoreceptors. It is reasonable to propose that the creation and maintenance of such an elaborate structure require unique functions within the distal CC (DCC) performed by specialized protein machinery not found in other primary cilia.

Because SPATA7 and the RPGR complex are functionally unique to the retina and their loss specifically disrupts the CC without impacting the TZ, SPATA7 is an ideal candidate to tease out differences between the TZ and the CC. To understand the photoreceptor-specific function of the TZ module proteins SPATA7, RPGRIP1, and RPGR, we investigated the CC substructure across multiple mouse models of syndromic and nonsyndromic retinal ciliopathy. Using a combination of mass spectrometry (MS) with cutting-edge superresolution microscopy and cryoelectron tomography (cryo-ET) imaging, we demonstrate for the first time the presence of two distinct zones within the CC: (1) the proximal CC (PCC), which is similar to the TZ of the primary cilium, and (2) the DCC, which is a photoreceptor-specific extension of the ciliary TZ. This specialized module of the photoreceptor sensory cilium plays an important role in maintaining the structure of the CC core, and consequently, mutations in *Spata7*, *Rpgr*, or *Rpgrip1* lead to DCC-specific defects.

Results

SPATA7 interacts with members of the NPHP–RPGR complex

In an effort to discern the functional significance of SPATA7 at the photoreceptor CC, we first sought to investigate its retina-specific interactions. Our previous research indicates that SPATA7 interacts with and is essential for the proper localization of RPGRIP1 (Eblimit et al., 2015). RPGRIP1 is known to directly interact with RPGR, whereas both of which interact with NPHP4 to form the RPGR complex (Hong et al., 2001; Murga-Zamalloa et al., 2010). Given the extensive protein interaction within the CC, we sought to further probe whether SPATA7 interacts with other members of the RPGR complex and other ciliopathy proteins. To this end, we performed immunoprecipitation (IP) followed by MS from *Spata7::GFP* bacterial artificial chromosome (BAC) transgenic mice. In these mice, the *Spata7::GFP* fusion protein functions as WT as it localizes to the CC and is sufficient to fully rescue retinal degeneration in the null mutant (Fig. S1). SPATA7::GFP IP from retinal extracts was performed with a high-affinity GFP nanobody that was subjected to MS. Over 160 candidate SPATA7-interacting proteins that displayed enrichment over the WT control were identified. Among them, 18 proteins showed a large enrichment (>100-fold) over the WT control (Fig. 1 a and Table S1). As expected, the previously known SPATA7-interacting protein RPGRIP1 was detected at >8,000-fold enrichment over the WT control. Furthermore, several known TZ proteins were also detected, including RPGR, NPHP1, NPHP4, and AHI1 (Fig. 1 a).

Given the localization of SPATA7 to the CC, candidate interactors that are known TZ module proteins were prioritized for further study. To confirm SPATA7 interaction with candidate proteins, we performed in vitro bimolecular fluorescence complementation (BiFC) assays. In these experiments, we quantified the fluorescence signals generated by complementation of interaction between C-terminal YFP-tagged bait protein (bait-VC) and N-terminal YFP-tagged SPATA7 (SPATA7-CVN). FACS-based quantification of YFP fluorescence in cells cotransfected with SPATA7-CVN and bait-VC displayed a significantly higher cell population that was positive for YFP signal compared with the negative controls (Fig. 1, b and c). These data indicate that SPATA7 directly interacts with components of the RPGR–NPHP complex, specifically RPGR, AHI1, NPHP1, NPHP4, and RPGRIP1.

SPATA7 interactors and other ciliopathy proteins display distinct localization patterns within the CC

Unlike other TZ genes, null mutations in *SPATA7*, *RPGRIP1*, or *RPGR* cause nonsyndromic retina-specific ciliopathies characterized by photoreceptor degeneration in patients (Meindl et al., 1996; Dryja et al., 2001; Wang et al., 2009). This tissue-specific phenotype is consistently recapitulated in corresponding mouse models (Hong et al., 2000; Zhao et al., 2003; Eblimit et al., 2015). To understand the underlying mechanism of this phenotype, we examined the immunolocalization of SPATA7, RPGRIP1, and RPGR proteins and other TZ markers at the CC of the mouse retina. We

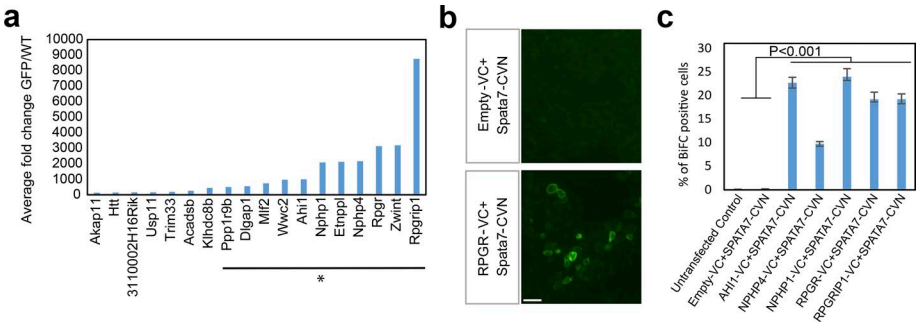

Figure 1. **SPATA7 interacts with members of the NPHP–RPGR complex. (a)** Distribution of mean GFP/WT Skyline peptide fold change of top candidate interacting partners of SPATA7 observed over three repeats. The asterisk signifies candidates that are enriched >1,000-fold in the GFP IP fraction in comparison with the WT control fraction. **(b)** The interaction between SPATA7 and representative RPGR was confirmed in vitro by the BiFC assay. HEK293T cells were transfected with either SPATA7-CVN alone (top) or together with RPGR-VC constructs (bottom). Strong fluorescence signals (green) were observed in cells expressing both SPATA7 and RPGR, which are quantified in c. Bar, 20 µm. **(c)** The percentage of BiFC-positive cells for all candidate-interacting partners that are known TZ module members was quantified by FACS (*t* test) in comparison with untransfected cells and SPATA7 alone. Error bars show means ± SEM.

used acetylated α-tubulin as a marker to label the tubulin-based cytoskeletal core of the cilium. At the photoreceptor CC, acetylated α-tubulin marked the entire CC, along with ∼0.2 µm of the microtubules extending into the outer segment. We observed that SPATA7, RPGRIP1, and RPGR were localized along the entire length of the CC (Fig. 2, a and b). We further assessed the CC localization of syndromic ciliopathy proteins (representatives of the NPHP–MKS complex), which are observed at the primary cilium TZ, including NPHP1, NPHP4, AHI1, MKS1, and SDCCAG8. Members of the NPHP complex that were observed to interact with SPATA7, including NPHP1 and NPHP4, showed protein localization throughout the entire CC, similar to SPATA7, RPGR, and RPG RIP1 (Fig. 2 b). In contrast, other TZ proteins such as MKS1 (MKS complex) and SDCCAG8 showed a distinct protein localization at the proximal end of the CC (Figs. 3 a and S3 a). Interestingly, AHI1, a protein that biochemically associates with the MKS proteins and genetically interacts with NPHP1, displays a localization pattern similar to NPHP–RPGR complex proteins at the CC (Fig. 2 b; Louie et al., 2010; Chih et al., 2011). Therefore, based on the localization of TZ protein at the CC, there appear to be two distinct subregions within the CC (Fig. 2 c): the PCC, housing all major TZ complexes including the NPHP, RPGR, and MKS complex, and the DCC, which houses photoreceptor-specific ciliary proteins SPATA7-RPGR-RPGRIP1 and their interactors.

Loss of SPATA7 results in mislocalization of the RPGR and NPHP proteins from the DCC region

Previously, we reported a loss-of-function *Spata7* mutant mouse model that displayed a rapid onset of photoreceptor degeneration recapitulating the human Leber congenital amaurosis phenotype (Eblimit et al., 2015). Immunofluorescence analysis of RPGRIP1 in the *Spata7* mutant retina displayed partial mislocalization from the CC to the photoreceptor cell body, suggesting a dependence on SPATA7 for its ciliary localization. Given that two distinct localization patterns were observed within the CC, we sought to more thoroughly analyze the role of SPATA7 in the localization of its interacting proteins (RPGR, AHI1, NPHP1, NPHP4, and RPG RIP1) to these subregions—particularly the DCC region—using immunofluorescence localization. To this end, we assessed *Spata7* mutant retinae at P15, a time point that precedes the onset of photoreceptor degeneration, displaying a largely normal retinal histology with intact CC and outer nuclear layers (Eblimit et al., 2015). Strikingly, compared with the WT localization along the entire ∼1.5-µm length of the CC, all interacting partners of SPATA7 were undetectable at the DCC region, whereas they retained localization at PCC (∼0.6 µm) in *Spata7* mutant photoreceptors (Fig. 2 d; quantified in Fig. 2 e). To further confirm whether these interactors are localized within the CC, we examined their localization at the basal body that was the immediate proximal region to the CC. Coimmunostaining of AHI1 and NPHP1 with the basal body marker γ-tubulin displayed a localization signal distal to the basal body, confirming that these interactors indeed localize within the CC (Fig. S3 b). On further assessment of the ciliary protein localization within the photoreceptor cell body, we observed that AHI1, which localizes to the CC, was now also detected within the photoreceptor cell body, specifically the outer nuclear layer region in the *Spata7* mutant (Fig. S4).

Because the CC subregions range from ∼500 nm (PCC) to ∼600 nm (DCC) in length, subciliary protein localization within these regions of the photoreceptor CC is not conclusive with conventional microscopy methods because of low resolution but rather requires more powerful techniques such as electron microscopy or more recently developed superresolution microscopy (Wensel et al., 2016). To assess the subciliary distribution of TZ proteins at the CC, we used a new application of stochastic optical reconstruction microscopy (STORM) in WT and *Spata7* mutant retinae. Consistent with our fluorescence immunolocalization results, STORM reconstruction of AHI1 signal at the CC of *Spata7* mutant rod cells (Fig. 2 f) revealed that AHI1 is restricted to the proximal end of the CC, in contrast with the full distribution in WT rod CC. This evidence suggests that SPATA7 is essential for localization of DCC proteins to the distal end of the CC.

The DCC is specifically disrupted in the absence of SPATA7

To determine the impact of SPATA7 loss on other key structures of the photoreceptor sensory cilium, we assessed the localization

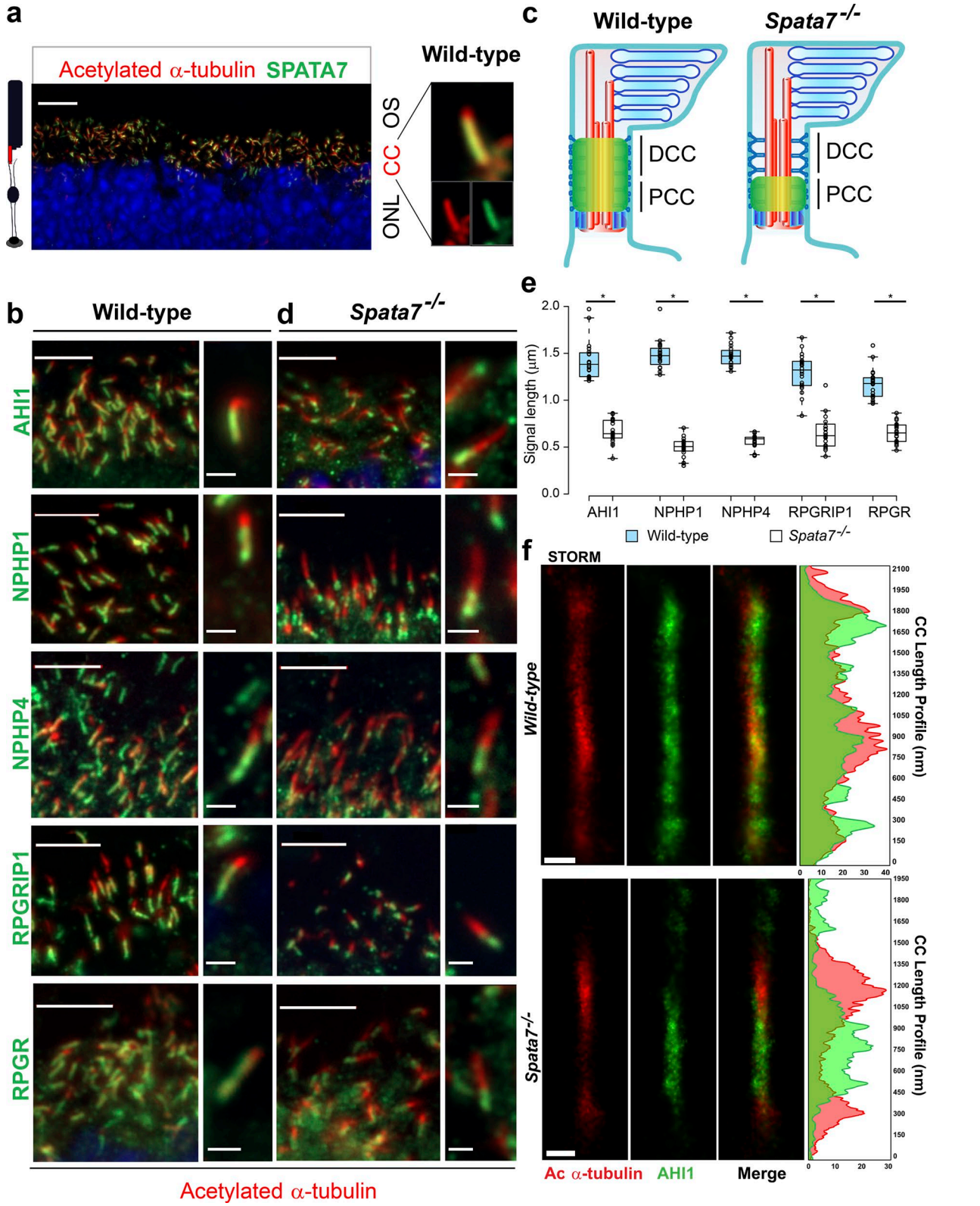

Figure 2. **Loss of SPATA7 leads to exclusion of its interacting proteins from the distal region of CC. (a)** Retinal cryosections (P15) were costained for SPATA7 (green) and acetylated α-tubulin (red) marking the entire CC of photoreceptors and ∼0.2 µm of the outer segment (OS). Single-cilium image shows localization of SPATA7 throughout the length of the CC. Bar, 10 µm. ONL, outer nuclear layer. **(b and d)** Immunofluorescence of retinal cryosections (P15) displaying localization of AHI1, NPHP1, NPHP4, RPGRIP1, and RPGR (green) at the CC marked by acetylated α-tubulin (red) in a WT (b) and *Spata7* mutant background (d). Representative single-cilium images display localization of the protein signal at the base of CC in the *Spata7* mutant (fourth column) in comparison with CC-wide localization in the WT retina (second column). Bars: (main images) 5 µm; (single-cilium images) 1 µm. **(c)** Model depicting the DCC and PCC within the CC of photoreceptor outer segments. **(e)** Box plots displaying IQRs of localization signal length for 20 cilia/protein in WT and *Spata7* mutant retinae across

of proteins that are normally housed in different structural modules of the sensory cilium, namely the PCC, the basal body, and the axoneme. First, proteins that localize specifically to the PCC region, namely MKS1 and SDCCAG8, were assessed in *Spata7* mutant retinae. In contrast with DCC proteins, PCC-resident proteins displayed normal localization within the CC in the absence of SPATA7 (Figs. 3 a and S3 a). In *Spata7* mutant retinae, the localization of C21ORF2, a basal body–resident protein, also remained unaffected (Fig. 3 b; Wheway et al., 2015). The axoneme of the sensory cilium extends beyond the CC and supports the outer segment disks in the photoreceptors. Axoneme marker RP1 decorates the microtubules of the outer segment and does not display overlap with CC proteins like RPGR (Liu et al., 2004). Consistent with previous literature, RP1 localized beyond the CC, displaying slight overlap with the tip of acetylated α-tubulin, which extended into ∼0.2 µm of the axoneme (Fig. 3 b). In the *Spata7* mutant retina, RP1 localization was unaffected and consistently decorated the outer segment axoneme (Fig. 3 b). Finally, we assessed a ciliary transporter protein that transiently shuttles between the inner segment and outer segment, IFT52, for localization at the sensory cilium of the *Spata7* mutant retina (Pazour et al., 2002). In contrast with SPATA7 and its interactors, IFT52 was detected at the basal body and retained its normal localization pattern in the *Spata7* mutant retina (Fig. 3 b). These data suggest that the absence of SPATA7 does not substantially impact the protein composition of PCC and other sensory cilium substructures.

To further test whether protein localization at the DCC can be disrupted by the loss of a PCC protein, we examined CC profile in the retina of *Sdccag8*^{mut} mice. Unlike DCC proteins, loss of *Sdccag8* causes syndromic ciliopathies such as Senior-Loken syndrome and Bardet-Biedl syndrome (Schaefer et al., 2011) with a component of retinal degeneration. We investigated the localization of DCC proteins AHI1, RPGR, and NPHP1 in the retinae of *Sdccag8*^{mut} mice. Despite the presence of significant background caused by retinal detachment in this mouse model, we observed that the localization pattern of these DCC proteins in rod cilia consistently remained unchanged (Fig. 3 c). Collectively, these data suggest that the mislocalization of SPATA7-interacting proteins in *Spata7* mutant retinae do not reflect a general CC defect but rather a specific loss of DCC integrity.

Loss of *Spata7* leads to microtubule destabilization in the DCC

The major distinction between the primary cilium and photoreceptor sensory cilium is the presence of an elaborate photoreceptor outer segment that anchors to the photoreceptor cell body via the CC. Since the distal end of the CC serves as the point of attachment to the outer segment, it is possible that the DCC provides structural stabilization, whereas the PCC acts as a sorting and transportation site, similar to its role in prototype primary cilium. In such a case, we hypothesize that structural defects of the CC would be expected in absence of the DCC proteins at the distal end. To test this hypothesis, we performed cryo-ET on isolated rod outer segment (ROS) fragments, which include the CC and a portion of the inner segment regions, from WT and *Spata7* mutant mice at P14. With this technique, ROS cilia were snap frozen for visualization of the 3D architecture of the CC in its biological state using EM tomography (Gilliam et al., 2012). In *Spata7* mutant ROS tomograms, the microtubule core of photoreceptor CC appeared fragile and consistently (across multiple tomograms from $n = 4$ P14 mice/genotype) displayed unraveling and flattening of the microtubule doublets in the DCC region compared with the tightly organized microtubule core in the WT (Fig. 4, a and b). As a result, the diameter of the cytoskeleton was wider at the DCC (WT radius, 203 nm; *Spata7* mutant radius, 393 nm) in comparison with the PCC region (WT radius, 183 nm; *Spata7* mutant radius, 238 nm; Fig. 4 [c and e] vs. Fig. 4 [d and f]). The basal body substructures were relatively intact in *Spata7* mutant ROS fragments except for a marked tendency to be flattened. This microtubule-unraveling phenotype could also be clearly observed by examining the 3D architecture of the DCC and PCC regions of the *Spata7* mutant photoreceptor CC (as shown in Video 1).

Given that the microtubule core in the *Spata7* mutant was destabilized and unraveled in the distal CC, we hypothesized that proteins housed inside the lumen of microtubule core of the CC such as centrin-2 (Giessl et al., 2004) would also be affected. In the photoreceptor sensory cilium, centrin-2 is uniquely localized along the entire length of the CC in contrast with the primary cilium, where it is largely restricted to the centrioles. Although this localization pattern was consistently observed in the WT photoreceptors, centrin-2 immunostaining was significantly reduced in the DCC in *Spata7* mutant photoreceptors (Fig. 5, a and b). This mislocalization phenotype was recapitulated with the STORM technique, where the centrin-2 distribution was clearly excluded from the *Spata7* mutant DCC (Fig. 5 c), thereby supporting our hypothesis of destabilization of the microtubule core in the DCC of the *Spata7* mutant photoreceptors.

Cep290 as a downstream effector of *Spata7*

Although the loss of SPATA7 leads to mislocalization of its interactors from the DCC, it is unclear how this results in microtubule destabilization in the DCC core as its interactors are not known to play a structural role. Hence, we questioned whether other ciliary proteins that are likely to play a structural role, such as CEP290, are affected in the *Spata7* mutant. CEP290 is the proposed protein component of the dense proteinacious Y-links that connect the axoneme microtubules to the ciliary membrane in both *Chlamydomonas reinhardtii* flagella and primary cilia (Craige et al., 2010; Drivas et al., 2013). In the mouse retina, we determined that CEP290 localized to both the DCC and PCC in P15 WT photoreceptors (Fig. 6 a). In the *Spata7* mutant photoreceptors, however, CEP290 was absent from the DCC region, whereas it normally localized at the base of the CC in a restricted fashion similar to the DCC proteins (Fig. 6, a and b). This distribution

three repeats (*, $P < 0.0001$; unpaired *t* test). The whiskers extend to data points that were <1.5× IQR away from first/third quartiles. **(f)** Representative 2D STORM reconstruction of the CC displaying AHI1 (green) and acetylated α-tubulin (red) in the WT (top) and *Spata7* mutant retina (bottom). The intensity of individual fluorophores was plotted along the length of the CC to determine the length of overlap between AHI1 signal and CC (rightmost panel). Bars, 200 nm.

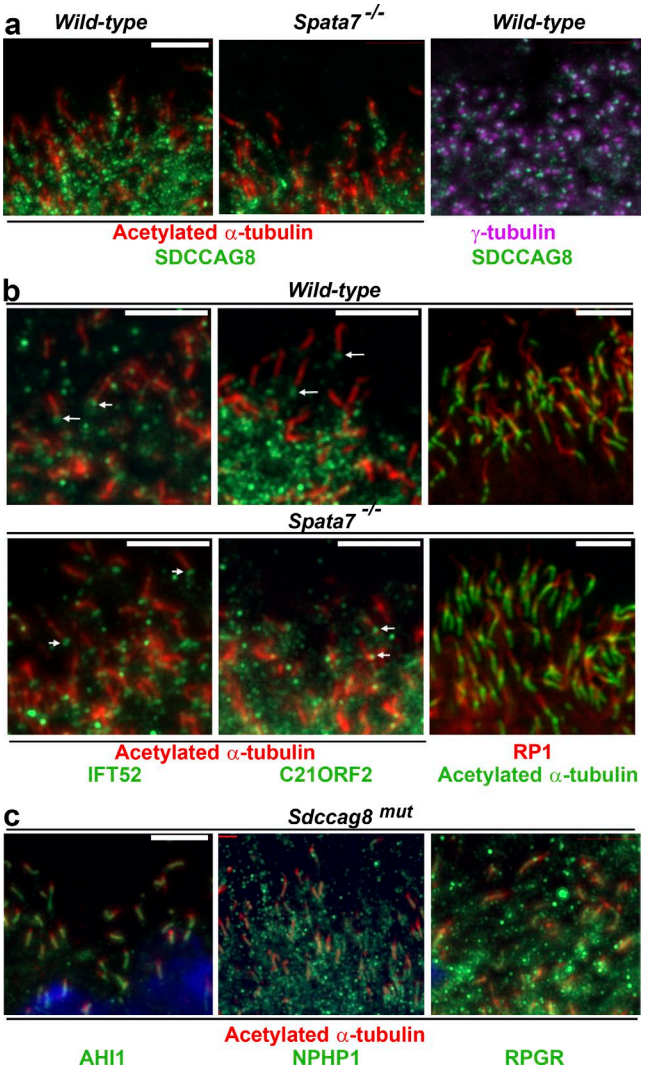

Figure 3. **The DCC is specifically disrupted in the absence of SPATA7.** **(a)** Immunohistofluorescence displaying localization of SDCCAG8 (green) and acetylated α-tubulin (red) marking the CC or γ-tubulin (purple) marking the basal body of the photoreceptor sensory cilium in WT and *Spata7* mutant retinae. **(b)** Retinal immunofluorescence displaying similar localization pattern in IFT52 and C21ORF2 (green) at basal body (as indicated by arrows) and RP1 at the axoneme in both WT and *Spata7* mutant retinae. **(c)** Immunohistofluorescence displaying localization of AHI1, NPHP4, and RPGR shown in green in the CC of *Sdccag8*^{mut} mice retinae (P15). Bars, 5 µm.

pattern was further confirmed by STORM reconstruction of CEP290 at the CC, in which CEP290 was primarily detected at PCC region (Fig. 6 c). Although CEP290 has not been detected as an interacting partner of SPATA7 in our IP–MS analysis, it has been reported to interact with RPGR, a DCC protein that directly interacts with SPATA7 (Rao et al., 2016). Hence, we hypothesize that SPATA7 and CEP290 may still functionally interact, perhaps mediated by RPGR complex members.

Given the potential indirect interaction between SPATA7 and CEP290 at the DCC, we further investigated genetic interactions between *Cep290* and *Spata7* genes. Specifically, we tested whether *Cep290* can act as a dominant modifier for the *Spata7* mutant retinal degeneration phenotype. *Cep290*^{rd16} is a recessive hypomorphic allele resulting in an in-frame deletion of 298 amino acids of *Cep290* that leads to a slow onset of retinal degeneration when homozygous (Chang et al., 2006). When one allele of *Cep290*^{rd16} was introduced in the *Spata7* mutant background, severe photoreceptor degeneration was evident as early as P20 with a significant reduction of the outer nuclear layer thickness (Fig. 6 d). This degeneration phenotype was much more severe than that of the *Spata7* mutant mice, which presented minimal photoreceptor loss at P20, indicating a strong in vivo genetic interaction between these two genes. Thus, CEP290 is a likely downstream effector of SPATA7 and its interacting partners.

SPATA7 is sufficient to apically extend the location of TZ proteins at the primary cilia

Our data demonstrate that the CC can be divided into DCC and PCC. The DCC houses a specialized subset of TZ proteins that extends beyond the PCC. Furthermore, SPATA7 is essential for the proper localization of RPGR, RPGRIP1, and other interactors at the DCC. However, the mechanism of inducing the apical extension of the RPGR complex beyond the TZ-like PCC to form the photoreceptor-specific DCC is not understood. Given the differential SPATA7 level among photoreceptor and other cell types, it is plausible that the high level of SPATA7 in photoreceptors is sufficient to drive the extension of its interacting TZ proteins into the DCC. To test this hypothesis, we examined whether moderate overexpression of SPATA7 in primary cilia is sufficient to apically extend the localization of SPATA7 interactors into the ciliary axoneme. We ectopically expressed SPATA7 fused to an N-terminal GFP tag in ciliated hTERT RPE-1 cells and evaluated the localization of endogenous AHI1. Endogenous expression of AHI1 was observed at the TZ of the primary cilium in hTERT-RPE1 cells (Fig. 7 a). Consistent with a previous study, modest SPATA7 overexpression was not restricted to the TZ of primary cilia but rather decorated the entire axoneme (Eblimit et al., 2015). Strikingly, we observed that the localization of AHI1 was shifted apically along the length of the ciliary axoneme upon expression of GFP-SPATA7 (Fig. 7 a). Further assessment of the endogenous expression of another TZ protein (RPGR complex member RPGRIP1L) consistently displayed apical extension along the ciliary axoneme in the presence of mild overexpression of SPATA7 (Fig. S5, a and b). This result demonstrates that modest overexpression of SPATA7 is sufficient to extend the TZ protein localization apically in the primary cilium. SPATA7 can thus serve as a key protein in inducing localization of other DCC proteins to apical regions of the CC.

Discussion

The photoreceptor CC has been classically defined as a homogenous, elongated structural homologue of the TZ present in the prototypic primary cilium. Although composed of similar biochemical modules as the TZ, it is unclear how a structurally elaborate CC is established and maintained within the photoreceptors. In this study, we have identified distinct protein localization patterns within the CC substructure using high-resolution microscopy on mouse models of photoreceptor ciliopathy. Based on the protein composition, we define two novel CC zones (Fig. 7 b): a PCC, which is similar to the TZ of the primary cilium and houses

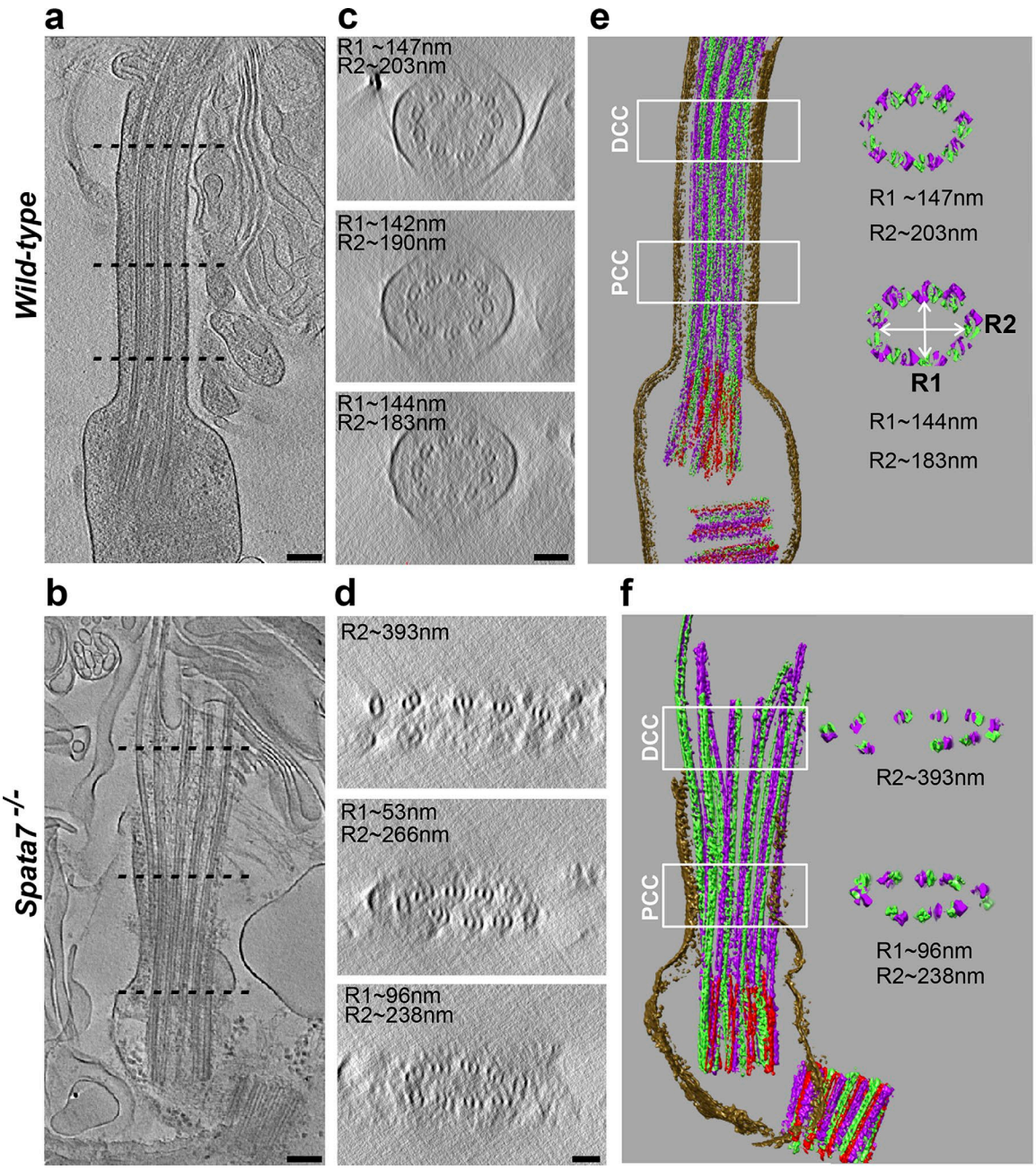

Figure 4. **Cryo-ET of isolated rods displaying microtubule destabilization in the DCC. (a and b)** Projections of tomogram slices showing CC from WT and *Spata7* mutant mice (n = 4 mice/genotype assessed at P14). Bars, 150 nm. **(c and d)** Tomogram projections of CC cross sections from WT (c) and *Spata7* mutant (d) mice. The cross-section views are along the z axis in the proximal-to-distal direction, with positions indicated by the horizontal lines in a and b displaying the PCC at the bottom and the most distal region at the top. Bars, 100 nm. **(e and f)** Segmented version of WT and *Spata7* mutant tomograms with continuous isodense surfaces colored as green (A-microtubule), purple (B-microtubule), and red (C-microtubule). Cross-sectional segments at the DCC and PCC regions are displayed on the right showing the intact complex at the PCC and a progressive unraveling of the microtubule core toward the DCC.

all major TZ complexes (NPHP, MKS, and RPGR), and a DCC zone spanning the distal two thirds of the CC, which is shown to be occupied by SPATA7 interactors. The DCC is structurally unique to the photoreceptor and is maintained by retina-specific ciliopathy protein, SPATA7, and its interacting partners RPGR and RPGRIP1. Loss of these key proteins, particularly SPATA7, leads to mislocalization of DCC proteins, which are essential for photoreceptor sensory cilium stability. Hence, this region acts as a photoreceptor-specific TZ (PSTZ; Fig. 7 b) within the CC. This study demonstrates that SPATA7 is not only essential for maintaining the integrity of the DCC but also plays a likely role in driving protein localization into the DCC. In vitro assays revealed that SPATA7 is sufficient for the apical translocation of the TZ proteins AHI1 and RPGRIP1L in primary cilia, suggesting that functionally, SPATA7 may be one of the key drivers that can induce an apical extension of TZ proteins within the photoreceptor sensory cilium. Consistent with this model, our data reveal physical interactions between SPATA7 and a panel of DCC proteins (RPGR, RPG

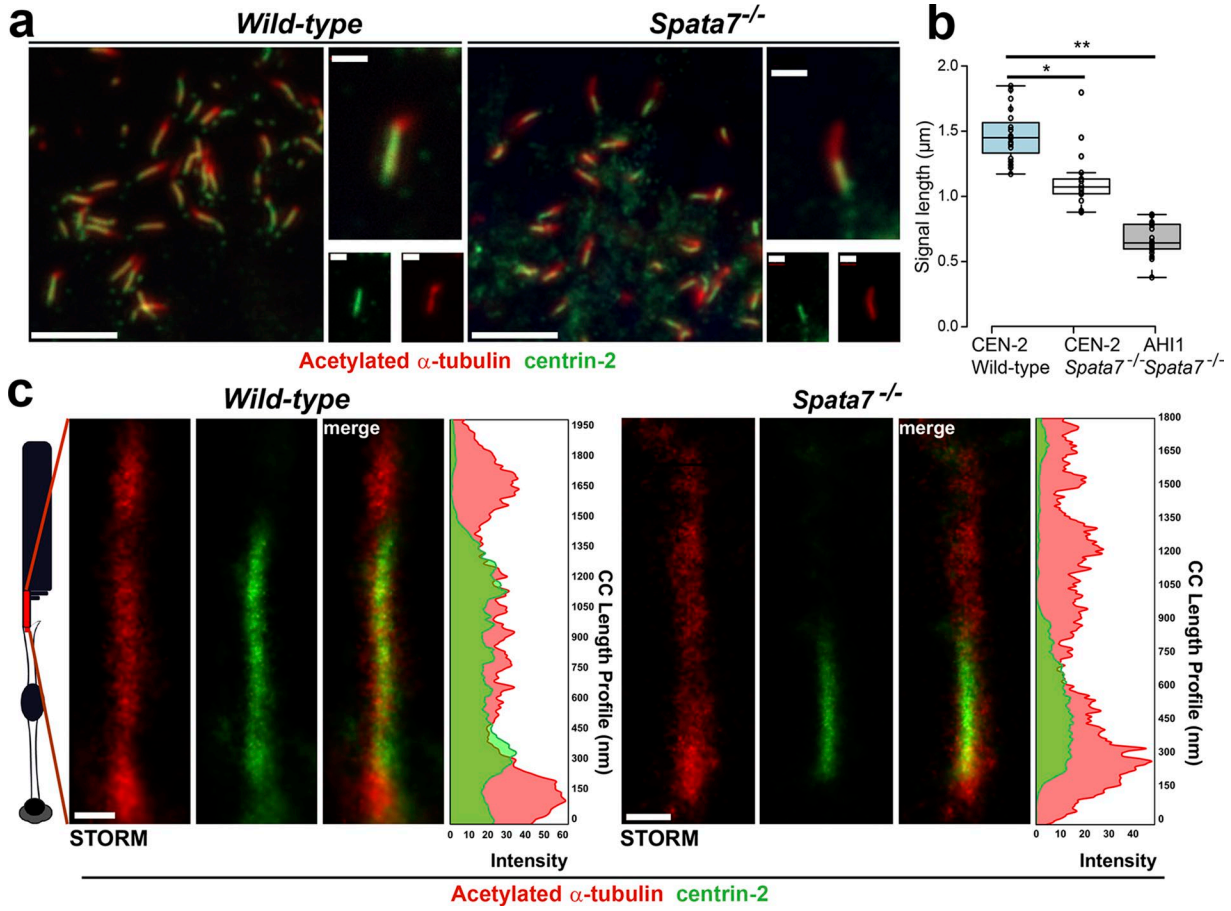

Figure 5. **Microtubule destabilization in the DCC leads to loss of centrin-2. (a)** Immunofluorescence images of retinal cryosections (P15) displaying localization of centrin-2 (green) and acetylated α-tubulin (red) marking the CC in WT and *Spata7* mutant background. Representative single-cilium image displays localization of the protein signal at the base of CC in the *Spata7* mutant. Bars: (main images) 5 µm; (single-cilium images) 1 µm. **(b)** Box plots display the IQR of localization signal length quantified for 20 cilia/protein in WT and *Spata7* mutant retina (*, **, P < 0.0001; unpaired *t* test). The whiskers extend to data points that were >1.5× IQR away from first/third quartiles. **(c)** Representative 2D STORM reconstruction of the CC displaying centrin-2 (green) and acetylated α-tubulin (red) in the WT (left) and *Spata7* mutant retinae (right) with localization length evident from the fluorophore intensity plots on the right. Bars, 200 nm.

RIP1, NPHP1, NPHP4, and AHI1), whereas protein components of PCC were not found among SPATA7 interactors such as SDCCAG8 (previously associated with the RPGR complex; Patil et al., 2012), MKS1, or other components of the MKS module (Table S1).

Sub-CC localization of TZ-module proteins has been observed in a few previous publications (Otto et al., 2010; Patil et al., 2012; Karlstetter et al., 2014). For example, in accordance with our model in which MKS module proteins localize to the PCC region, CC2D2A/MKS6 is observed at the proximal region of CC in a zebrafish model (Bachmann-Gagescu et al., 2011). However, the precise functional significance of such a sub-CC localization has not been investigated. This study provides the first functional evidence of DCC as a distinct region and highlights the specific role of SPATA7 in the localization of proteins to the DCC. The mislocalization phenotype observed in the *Spata7* mutant model suggests the presence of intermediate steps in the localization of ciliary proteins to CC. It is established that ciliary targeting of RPGR complex proteins to the CC is dependent on RPGRIP1 (Patil et al., 2012). In this study, we have established that although these proteins can successfully localize to the PCC (mediated at least in part by RPGRIP1), they depend on SPATA7 for their localization to the DCC. Hence, we propose that SPATA7 functions in conjunction with RPGRIP1 for proper localization and function of the DCC proteins.

The DCC in *Spata7* mutant photoreceptors displays an unraveled and disassociated microtubule core, indicating that the DCC proteins together structurally support the microtubule core and aid in a tight 9(2) + 0 formation in the DCC. The DCC lies immediately proximal to the outer-segment disk compartment. Consequently, destabilization of the DCC structure can impact ciliary transport and affect outer-segment disk renewal. In accordance, the previous investigation of *Spata7* mutant outer segment ultrastructure has displayed shortened and disorganized disk membranes, suggesting an impact of the flattening of DCC structure on disk formation (Eblimit et al., 2015). Although overexpressed SPATA7 decorates the cellular microtubule network in vitro (Fig. S5 c), it remains unclear whether SPATA7 directly mediates microtubule stability in the CC or acts through other microtubule-binding DCC proteins such as NPHP1, NPHP4, and RPGRIP1 (Mollet et al., 2005; Patil et al., 2012; Eblimit et al., 2015). Of particular interest is FAM161a, a microtubule-binding protein that localizes to the photoreceptor CC and basal body. Ultrastructural

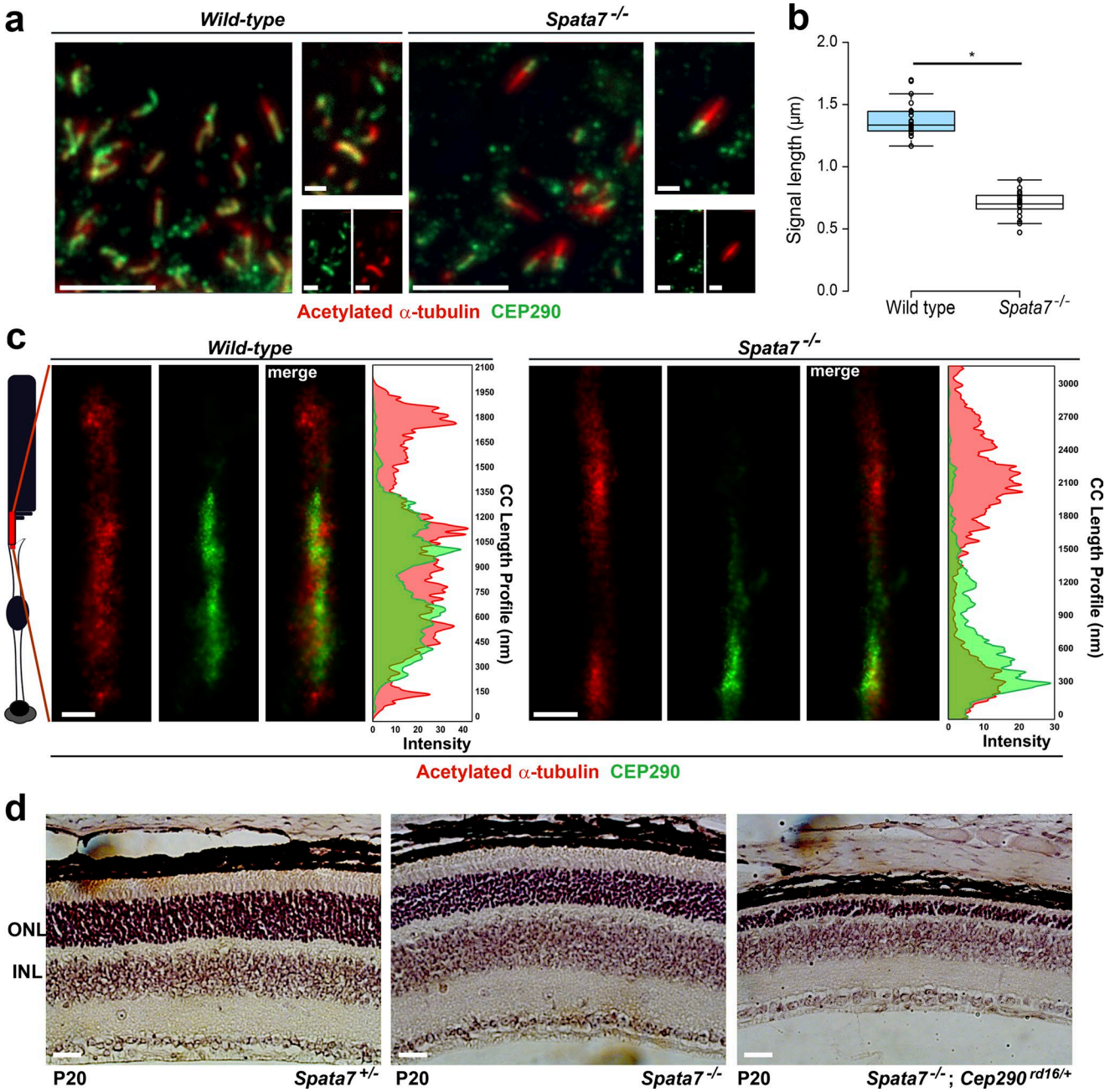

Figure 6. **Loss of Cep290, a putative protein component of Y-links, causes microtubule destabilization in *Spata7* mutant photoreceptors. (a)** Immunofluorescence images displaying localization of CEP290 (green) throughout CC marked by acetylated α-tubulin (red) in WT and reduction of localization signal to the PCC region in the *Spata7* mutant background. Bars: (main images) 5 µm; (single-cilium images) 1 µm. **(b)** Box plots display the IQR of CEP290 localization signal length quantified for 20 cilia/protein in WT and *Spata7* mutant retina (*, $P < 0.0001$). The whiskers extend to data points that were >1.5× IQR away from first/third quartiles. **(c)** Representative 2D STORM reconstruction of the CC displaying CEP290 (green) and acetylated α-tubulin (red) throughout the WT CC (left) and at the PCC region in the *Spata7* mutant retina (right) with localization length evident from the fluorophore intensity plots on the right. Bars, 200 nm. **(d)** Hematoxylin and eosin (H&E) staining of paraffin-embedded retinal sections from *Spata7*$^{+/-}$, *Spata7*$^{-/-}$, and *Spata7*$^{-/-}$;*Cep290*$^{rd16/+}$ background assessed at P20 display severe loss of photoreceptor nuclei (outer nuclear layer [ONL]) on a *Spata7*$^{-/-}$;*Cep290*$^{rd16/+}$ background. Bars, 20 µm. INL, inner nuclear layer.

analysis of the photoreceptors in the Fam161a(GT/GT) mouse displays microtubule destabilization at the DCC similar to that observed in the *Spata7* mutant mouse. However, it also shows several phenotypes, including shortening of the ciliary length, RP1 mislocalization, reduction in PRPH2 housed in the outer segment, and perpendicular orientation of the outer-segment disks that are inconsistent with the *Spata7* model (Karlstetter et al., 2014). Given the DCC core destabilization phenotype in the FAM161a mouse model, it serves as an interesting candidate DCC protein that may play a similar role as SPATA7–RPGR–NPHP proteins in the CC, warranting further investigation.

In conclusion, our study provides the evidence of a novel PSTZ at the distal end of CC. Loss of key DCC proteins such as SPATA7 along with RPGR–NPHP complex members results in

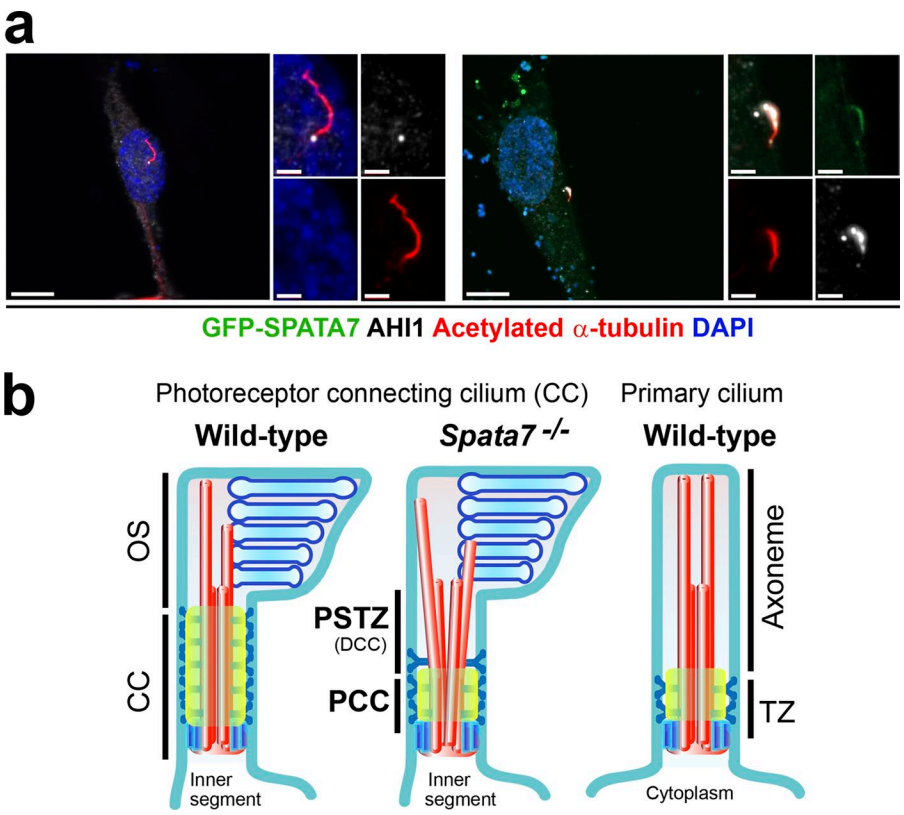

Figure 7. **SPATA7 extends AHI1 localization apical of the TZ in primary cilia. (a)** Endogenous AHI1 (white) localizes at the TZ of the primary cilium, marked by acetylated α-tubulin in hTERT-RPE1 cells (left). Ectopic expression of hSPATA7-GFP (right) induces apical extension of the endogenous AHI1 localization signal beyond the TZ into the ciliary axoneme (subsets display zoomed images of AHI1 [white], acetylated α-tubulin [red], SPATA7-GFP, and DAPI). Bars: (main images) 10 µm; (insets) 2 µm. **(b)** Model displaying the CC zones PSTZ at the DCC and PCC that are visible in the *Spata7* mutant retinae. The CC is comprised of PCC, a region homologous to the TZ of the primary cilium, and PSTZ, a specialized photoreceptor-specific zone of the CC that is crucial for maintenance of the CC microtubule core. OS, outer segment.

destabilization of the axonemal structure and ultimately photoreceptor degeneration. Characterization of this photoreceptor-specific ciliary subregion provides a new mechanistic explanation for the retinal-specific phenotypes caused by mutations in the ciliopathy gene *SPATA7* and its interacting *RPGR* as well as *RPGRIP1* genes. Given the highly specialized nature of the sensory cilium, further studies focusing on these primary cilia specializations can improve our understanding of mechanisms underlying the pleiotropic presentation of ciliopathy phenotypes.

Materials and methods

Animal breeding, mouse models, and genetic interaction

All animals were handled in accordance with the policies on the treatment of laboratory animals by Institutional Animal Care and Use Committee of Baylor College of Medicine. Mice were housed on a standard diet and in a 12-h light to 12-h dark cycle. For all experiments, P15 *Spata7* (Eblimit et al., 2015) mutant mice were compared with age-matched WT C57BL6/J mice unless otherwise specified. Although high expression of *Spata7* was observed in the testis, there were no fertility issues observed in the mutants. To generate the EGFP-tagged *Spata7* transgenic mice, an EGFP cDNA was inserted immediately before the *Spata7* stop codon of a BAC containing the entire *Spata7* gene. A linearized BAC DNA vector was injected into C57 mouse embryos in the Genetically Engineered Mouse core facility at Baylor College of Medicine. Transgene expression was characterized by immunohistochemistry. The *Spata7*-EGFP transgene appeared to be expressed at physiological levels with the same expression pattern as the endogenous *Spata7* gene in the mouse retina. The following primer pair was used for genotyping: forward, 5′-AACCTCTGTGGATGT CATTGAAG-3′; and reverse, 5′-AGAAGTCGTGCTGCTTCATGT-3′. The *SDCCAG8*^{mut} mice line (OVE2161B-CA1C-2; Sdccag8; 017598; The Jackson Laboratory; a gift from P. Overbeek, Baylor College of Medicine, Houston, TX) was generated by using the Sleeping Beauty transposon transgenic approach. These mice harbored a mutation created by random insertion of the pT2-BART3 transposon. The donating investigator reported that the integration site was in the intron after exon 12 of the serologically defined colon cancer antigen 8 gene (*Sdccag8*) on chromosome 1 using inverse PCR analysis. The transgene is linked to the + strand at position 178,833,225 bp (NCB137/mm9; L:SV40:178,833,225^{+}). The *Sdccag8* transcript was not detected in mice homozygous for this insertion. *SDCCAG8*$^{mut/mut}$ offspring were observed at lower-than-predicted Mendelian ratios. All homozygous mice exhibited cleft palates with an open palate observed by E15. For genetic interactions, *Spata7* mutant mice (on a C57BL6/J background; Eblimit et al., 2015) were crossed with B6.Cg-*Cep290rd16*/Boc (*Cep290rd16/rd16*; procured from The Jackson Laboratory on a C57BL6 background) to generate *Spata7*$^{-/-}$; *Cep290*$^{rd16/+}$ mice.

IP and liquid chromatography (LC)–tandem MS (MS/MS) analysis

For coimmunoprecipitation experiments, retinae from five adult *Spata7*-GFP transgenic and five adult WT mice (per replicate across three replicates) were lysed in the IP buffer (20 mM Tris, pH 7.5, 1 mM EDTA, 150 mM NaCl, 0.5% NP-40, and protease inhibitor cocktail tablets [11836170007; Roche]) by homogenization followed by sonication. The lysates were precleared using binding control beads (bab-20; ChromoTek) followed by

IP with GFP–trap-A (gta-20; ChromoTek) beads. After washes, beads were boiled in 20 µl of 1× NuPAGE lithium dodecyl sulfate sample buffer (Invitrogen) and subjected to SDS-PAGE (NuPAGE 10% Bis-Tris gel; Invitrogen). The eluted proteins were visualized with Coomassie brilliant blue and excised into gel pieces according to molecular size. Individual gel pieces were destained and subjected to in-gel digestion using trypsin (T9600; GenDepot). Tryptic peptides were resuspended in 10 µl loading solution (5% methanol containing 0.1% formic acid) and subjected to nanoflow LC-MS/MS analysis with a nano-LC 1000 system (Thermo Fisher Scientific) coupled to an Orbitrap Elite (Thermo Fisher Scientific) mass spectrometer. The peptides were loaded onto a Reprosil-Pur basic C18 high-performance liquid chromatography precolumn (1.9 µm; Dr. Maisch GmbH) that was 2 cm × 100 µm in size. The precolumn was switched in-line with an in-house 50 mm × 150 µm analytical column packed with Reprosil-Pur basic C18 equilibrated in 0.1% formic acid/water. Peptides were eluted using a 75-min discontinuous gradient of 4–26% acetonitrile/0.1% formic acid at a flow rate of 700 nl/min. The eluted peptides were directly electrosprayed into an Orbitrap Elite mass spectrometer operated in the data-dependent acquisition mode acquiring fragmentation spectra of the top 25 strongest ions and under the direct control of Xcalibur software (Thermo Fisher Scientific).

Database search and data validation

Obtained MS/MS spectra were searched against the target-decoy mouse RefSeq database in the Proteome Discoverer 1.4 interface (Thermo Fisher Scientific) with the MASCOT algorithm (2.4; Matrix Science). The precursor mass tolerance was confined within 20 ppm with fragment mass tolerance of 0.5 D and a maximum of two missed cleavages allowed. Dynamic modification of oxidation, protein N-terminal acetylation, and destreak was allowed. The peptides identified from the MASCOT result file were validated with a 5% false discovery rate and subjected to manual verifications for correct assignment.

Protein quantification

The intensity-based absolute quantification (iBAQ) algorithm was used to calculate protein abundance to compare the relative amounts of different proteins in the sample. Simply, iBAQ was calculated based on normalization of summed peptide intensity divided by the number of theoretically observable tryptic peptide of a certain protein. The PD1.4 result file and the RAW file from MS was then imported to Skyline software to carry out manual relative quantification (Fig. S2). Each individual peptide was validated by checking for its ID from the PD1.4 result, and the missing peptides were selected by the match-by-run approach. The area under the curve for each peak was adjusted based on the retention time. Finally, the sum of the area under the curve of all precursor ions (for each peptide) was calculated.

BiFC

The BiFC assay was performed as previously described (Chen et al., 2007). In brief, cDNAs from genes encoding candidate SPATA7-interacting proteins (RPGR, AHI1, NPHP1, NPHP4, and RPGRIP1) were cloned in the bait-VC and cotransfected with *SPATA7* construct tagged with SPATA7-CVN. Constructs expressing SPATA7-CVN (the N terminus of Venus YFP) and bait-VC (the C terminus of Venus YFP) were transfected into 293T cells. After 48 h, fluorescence signals generated by the complementation between N- and C-terminal YFP as a result of SPATA7 binding with its interacting partner was visualized using fluorescence microscopy and quantified by FACS. Cells expressing only SPATA7-CVN or empty vector were used as controls.

Immunofluorescence

For evaluation of protein localization in photoreceptor cells of WT and *Spata7* mutant mice, unfixed eyes of 14-d-old mice were harvested and snap frozen in cryoembedding optimal cutting temperature medium at −80°C. Retinal sections were fixed and subsequently treated with blocking buffer (10% normal goat serum in PBS + 0.1% Triton X-100) for 1 h. Sections were then incubated overnight at 4°C with corresponding primary antibodies (Table S2) diluted in blocking buffer. Species-specific fluorescently conjugated secondary antibody (Bethyl Labs) in blocking buffer was applied, followed by washes in PBS. To avoid bleedthrough and cross-emission, Al-488 (excitation wavelength spectrum, 400–530 nm) and Cy5 (wavelength spectrum, 545–700 nm) were used as secondary antibodies with well-separated spectral profiles. Sections were counterstained with DAPI (1 µg/ml) and mounted using ProLong Gold antifade reagent (Thermo Fisher Scientific). For GFP staining, we used paraffin-embedded retinal sections as described previously (Li et al., 2013). Representative images were acquired on AxioObserver Z.1 inverted fluorescence microscope with Apotome.2-based optical sectioning and structured illumination on a 100× enhanced chemiluminescence Plan Apochromat objective (ZEISS). Images were processed with Zen 2 core software (ZEISS). To observe the localization of proteins within the CC, image stacks were taken with a z distance spanning the entire length of CC (using acetylated α-tubulin as a reference for the CC) and projected as a maximum-intensity image followed by length measurement using the Zen 2 core software measurement module. Measurements for 20 cilia per genotype were recorded across three repeats. CC that were present in a region of high background or in a retinal segment overlaying the outer nuclear layer were not assessed for localization signal length as the background interfered with proper length assessment. Ciliary axonemes were imaged with the Cy5 fluorophore (unless otherwise specified) and false colored to exhibit red cilia in the image.

Immunocytochemistry

The hTERT-RPE1 cells were grown on 12-well plates until reaching 90% confluency. To induce cilia growth, cells were fed with serum-starvation medium (DMEM/F12; 0.2% FCS + 1% penicillin/streptomycin + 1% sodium pyruvate). 24 h after starvation, cells were transfected with DNA plasmids using Lipofectamine 2000 (Invitrogen) with a 1:2.5 ratio as per the manufacturer's instructions. 24 h after transfection, cultured cells were fixed with 2% PFA for 20 min at RT followed by 1% Triton X-100 treatment for 3 min and blocking with 2% BSA for 20 min. Subsequently, cells were incubated with primary antibodies (anti-RPGRIP1L [guinea pig; 1:500; SNC040], anti-AHI1 [rabbit; 1:200], mouse anti-FLAG [1:500; F3165; Sigma-Aldrich], and mouse antiacetylated α-tubulin antibody [1:200; Sigma-Aldrich]) diluted in blocking

solution for 1 h. After incubation, cells were washed three times with PBS and incubated with the corresponding Alexa Fluor–conjugated secondary antibody (Thermo Fisher Scientific or Molecular Probes). Finally, slides were washed three times in PBS for 5 min and mounted in ProLong Gold mounting medium (Invitrogen). Cells that displayed destabilization of the cytoskeleton caused by very high levels of ectopic SPATA7 expression were excluded from analysis (Fig. S5 c).

STORM immunofluorescence and resin embedding

P15 mouse retinae from either *Spata7* mutant mice or WT controls were immunolabeled as a whole retina in solution for STO RM following a two-step protocol. First, retinae were dissected unfixed in ice-cold Ames's medium (Sigma-Aldrich) and blocked with 10% normal goat serum + 0.3% saponin + 1× protease inhibitor cocktail (GenDepot) diluted in 1× Ames's medium for 2 h at 4°C. Unfixed labeling of the retina is necessary for complete antibody penetration to the CC axoneme as described previously (Evans et al., 2010; Hidalgo-de-Quintana et al., 2015). Primary antibodies (5–10 µg) were added to blocking buffer and incubated at 4°C for 20–22 h. Retinae were washed three times for 5 min in 2% normal goat serum in Ames' medium on ice before secondary antibodies (Fab2 goat anti–mouse IgG Alexa Fluor 647 and Fab2 goat anti–rabbit IgG Alexa Fluor 555; Thermo Fisher Scientific) were added in the same buffer and incubated at 4°C for 2 h. Retinae were washed in 2% next-generation sequencing (NGS)/Ames's medium six times for 5 min each on ice and fixed in 4% formaldehyde diluted in 1× PBS for 15 min.

Next, retinae were reblocked in 10% normal goat serum + 0.2% Triton X-100 (diluted in 1× PBS) for 2 h at RT. Primary antibodies (10 µg each) were read to the blocking buffer and incubated for 2 d at 4°C. This second immunohistochemistry step featured Triton permeabilization to assure complete antigen binding in and around the CC. After the second primary antibody incubation, retinae were washed 4× for 10 min each in 2% NGS/1× PBS. The same secondary antibodies were added to the wash buffer as before (8 µg each) for overnight incubation at 4°C. Retinae were washed 6× in 2% NGS/1× PBS for 5 min each before postfixation in 3% formaldehyde diluted in 1× PBS for 1 h at RT.

The resin-embedding protocol for immunolabeled retinae is based on previous studies (Kim et al., 2015; Sigal et al., 2015). Postfixed retinae were dehydrated in a series of ethanol washes (15 min each: 50%, 70%, 90%, 100%, and 100%) followed by embedding steps of increasing concentrations with UltraBed Epoxy resin (Electron Microscopy Sciences) to ethanol (2 h each; 25:75%, 50:50%, 75:25%, and 100% resin twice). Embedded retinae were cured on the top shelf of a 65°C baking oven for 20 h. 1-µm sections were cut on a UCT or UC6 ultramicrotome (Leica Biosystems) and dried directly onto glass-bottomed dishes (35 mm; No. 1.5 coverslips; MatTek Corporation).

STORM image acquisition

Immediately before imaging, 10% sodium hydroxide (wt/vol) was mixed with 200-proof ethanol for 30 min to prepare a mild sodium ethoxide solution. Glass-bottomed dishes with ultra-thin retina sections were immersed for 30–40 min for chemical etching of the resin that facilitates STORM in this preparation (Kim et al., 2015; Sigal et al., 2015). Etched sections were then washed and dried on a 50°C heat block. The following STORM imaging buffer was prepared: 50 mM Tris, pH 8.0, 10 mM NaCl, oxygen scavenging system (0.56 mg/ml glucose oxidase and 34 µg/ml catalase [Sigma-Aldrich]), 10% (wt/vol) glucose, 15 mM ethanolamine, and 10% VectaShield (Vector Laboratories). Imaging buffer was added onto the dried, etched sections, which were sealed with another No. 1.5 coverslip for imaging.

Imaging was performed on a Nikon N-STORM system, which features 100× CFI Apochromat total internal reflection fluorescence 100× 1.49 NA oil objective on an inverted Nikon Ti Eclipse microscope featuring a quad cube filter (zt405/488/561/640 m-TRF; Chroma Technology Corp) and a Piezo z stage with the Perfect Focus System for z stability. A laser combiner (MLC400B; Agilent Technologies) with acoustooptic tunable filter modulation housed the 200-mW 561-nm and 647-nm solid-state lasers that were used for imaging in this study. STORM image acquisition was controlled by NIS Elements AR software (Nikon). For each STORM acquisition, a 512 × 512–pixel field was captured by an iXon DU897 electron-multiplying charge-coupled device camera (Andor Technology; each pixel was 160 nm wide for a ∼40-µm^2 STORM area), and a 3D cylindrical lens was inserted into the light path. Chromatic aberration between channels was corrected via an x–y warp calibration.

Ultra-thin sections were first scanned with low–laser power excitation to locate a region with multiple well-stained CC. From this region, differential interference contrast images and low-power laser images were saved as a reference. Both the 561- and 647-nm laser lines were increased to maximum power to initiate photoswitching before imaging frames were collected (∼56 frames per second). 20,000–50,000 frames were collected for each imaging experiment. 561-nm and 647-nm frames were collected sequentially without any activation frame (also termed direct STORM).

STORM analysis

Analysis of STORM acquisition frames was performed using NIS Elements AR analysis software. For each experiment, individual photoswitching events were analyzed and selected as molecules to be included as 2D Gaussian data points within reconstructed images. Selection varied in peak minimum intensity from 400–1,000 based on the quality of photoswitching. To further assess reconstruction quality and Gaussian localization accuracy, a calculation for error in localization (Thompson et al., 2002) was considered for each reconstructed CC Gaussian cluster (defined as a selected region of interest surrounding a CC and surrounding structures). For these clusters, a mean localization accuracy per molecule of <20 nm was used as a benchmark for good STORM reconstruction and acceptable superresolution imaging. A local density filter (20-molecule thresholding value and 50–100-nm radius) was used in reconstructions with a considerable background. Cilia clusters were processed in FIJI (ImageJ; National Institutes of Health), and the Straighten tool was applied to straighten curved or bent cilia to acquire comparable length profiles. Lookup tables within the analysis software were removed from all reconstructions to limit the saturation of strong Gaussians points; however, whole-image contrast was adjusted for clarity when necessary.

Cryo-ET

For cryo-ET, a 3-µl drop of the specimen (isolated rod outer segment/inner segment preparation; isolated as described previously [Gilliam et al., 2012; Wensel et al., 2016]) was applied to a glow-discharged 200 mesh holey carbon grid (Quantifoil Micro Tools GmbH). The preparations from the WT and *Spata7* mutant retinae were processed in parallel to avoid technical artifacts. The grids were flash frozen and plunged into liquid ethane at liquid nitrogen temperature using a Vitrobot (FEI) or EM GP (Leica Microsystems) freezing device with blotting from the opposite side from that used for sample application to minimize flattening and breaking of cilia. The grids containing cell samples in vitreous ice were imaged at 12,000× magnification in a JEM2100 electron microscope (JEOL) at 200 kV using Serial EM software (Mastronarde, 2005) to collect a tilt series. The tilt series were collected between ±60° at 2° increments with a cumulative dose of 70–90 e/Å-2 at ∼10 µm defocus using a 4,000 × 4,000 charge-coupled device camera (Gatan). The 3D reconstruction of the tomograms was performed with IMOD software (Kremer et al., 1996). Features of interest from tomograms were manually selected and segmented using Avizo (FEI) and visualized using the Chimera 3D software package (Pettersen et al., 2004).

Statistical information

All error bars in graphical figures display SEM. Statistical comparison in cilia protein localization length was performed by unpaired *t* test using Prism (GraphPad Software). This signal length comparison data are displayed as box and whisker plots displaying the interquartile range (IQRs) with overlaying data points. The whiskers extend to data points that are <1.5× IQR away from first or third quartiles. Outliers are defined as data points that fall below Q1 − 1.5 IQR or above Q3 + 1.5 IQR.

Online supplemental material

Fig. S1 displays rescue and localization of *Spata7*::GFP transgenic expression. Fig. S2 displays MS1 peptide area used for Skyline manual quantification. Fig. S3 displays localization of MKS1, AHI1, and NPHP1 at the photoreceptor CC of WT and *Spata7* mutant photoreceptor CC. Fig. S4 displays AHI1 localization in *Spata7* mutant mouse photoreceptor cells. Fig. S5 displays apical translocation of RPGRIP1L in the presence of mild overexpression of SPATA7 in hTERT-RPE1 cells and also cytoskeletal destabilization observed in the majority of cells with high ectopic expression of SPATA7. The Skyline, iBAQ, and peptide fold change values obtained from MS analysis can be found in Table S1 for top interacting candidates and all interactors (Sheets 1 and 2). A list of antibodies, their specific conditions, and dilutions used are cataloged in Table S2. Video 1 displays the 3D architecture of the DCC and PCC regions of the Spata7 mutant photoreceptor CC.

Acknowledgments

We thank Matthew Dougherty for assistance in the visualization of cryo-ET data.

This project was funded by the Retina Research Foundation of the National Eye Institute grants R01EY022356 (to R. Chen), R01EY020540 to (G. Mardon and R. Chen), R01EY026545 and R01EY07981 (to T.G. Wensel), and F32EY027171 (to M.A. Robichaux); the European Commission's Seventh Framework Programmes FP7/2009 under grant 241955 (SYSCILIA; to R. Roepman), and by the Netherlands Organization for Scientific Research NWO Vici-865.12.005 (to R. Roepman).

The authors declare no competing financial interests.

Author contributions: R. Dharmat designed the study, performed the experiments, interpreted the results, and wrote the paper. R. Dharmat, A. Eblimit, M.A. Robichaux, Z. Zhang, T.-M.T. Nguyen, F. He, A. Jain, and Y. Li performed the experiments and analyzed the data. R. Dharmat performed the immunofluorescence, IP, mouse, and cell line experiments, collected the data, and analyzed the results. A. Eblimit performed the mouse experiments including generation of GFP-Spata7 transgenic and CEP290 lines, and M.A. Robichaux performed the STORM experiments and edited the manuscript. A. Jain performed MS, which was analyzed by S.Y. Jung and J. Qin. P. Overbeek made the *SDCCAG8* mutant mouse. T.-M.T. Nguyen performed the cell line immunofluorescence work under the supervision of R. Roepman. F. He and Z. Zhang performed the cryotomography, collected the data, and analyzed the results with T.G. Wensel. T.G. Wensel and G. Mardon helped to refine the hypothesis, interpreted the results, and edited the manuscript. R. Chen conceived and supervised the research, interpreted the results, and wrote the paper. All authors have read and accepted the manuscript.

Submitted: 19 March 2018
Revised: 9 May 2018
Accepted: 23 May 2018

References

Bachmann-Gagescu, R., I.G. Phelps, G. Stearns, B.A. Link, S.E. Brockerhoff, C.B. Moens, and D. Doherty. 2011. The ciliopathy gene cc2d2a controls zebrafish photoreceptor outer segment development through a role in Rab8-dependent vesicle trafficking. *Hum. Mol. Genet.* 20:4041–4055. https://doi.org/10.1093/hmg/ddr332

Cevik, S., A.A.W.M. Sanders, E. Van Wijk, K. Boldt, L. Clarke, J. van Reeuwijk, Y. Hori, N. Horn, L. Hetterschijt, A. Wdowicz, et al. 2013. Active transport and diffusion barriers restrict Joubert Syndrome-associated ARL13B/ARL-13 to an Inv-like ciliary membrane subdomain. *PLoS Genet.* 9:e1003977. https://doi.org/10.1371/journal.pgen.1003977

Chang, B., H. Khanna, N. Hawes, D. Jimeno, S. He, C. Lillo, S.K. Parapuram, H. Cheng, A. Scott, R.E. Hurd, et al. 2006. In-frame deletion in a novel centrosomal/ciliary protein CEP290/NPHP6 perturbs its interaction with RPGR and results in early-onset retinal degeneration in the rd16 mouse. *Hum. Mol. Genet.* 15:1847–1857. https://doi.org/10.1093/hmg/ddl107

Chen, L.-Y., D. Liu, and Z. Songyang. 2007. Telomere maintenance through spatial control of telomeric proteins. *Mol. Cell. Biol.* 27:5898–5909. https://doi.org/10.1128/MCB.00603-07

Chih, B., P. Liu, Y. Chinn, C. Chalouni, L.G. Komuves, P.E. Hass, W. Sandoval, and A.S. Peterson. 2011. A ciliopathy complex at the transition zone protects the cilia as a privileged membrane domain. *Nat. Cell Biol.* 14:61–72. https://doi.org/10.1038/ncb2410

Craige, B., C.-C. Tsao, D.R. Diener, Y. Hou, K.-F. Lechtreck, J.L. Rosenbaum, and G.B. Witman. 2010. CEP290 tethers flagellar transition zone microtubules to the membrane and regulates flagellar protein content. *J. Cell Biol.* 190:927–940. https://doi.org/10.1083/jcb.201006105

Drivas, T.G., E.L.F. Holzbaur, and J. Bennett. 2013. Disruption of CEP290 microtubule/membrane-binding domains causes retinal degeneration. *J. Clin. Invest.* 123:4525–4539. https://doi.org/10.1172/JCI69448

Drummond, I.A. 2012. Cilia functions in development. *Curr. Opin. Cell Biol.* 24:24–30. https://doi.org/10.1016/j.ceb.2011.12.007

Dryja, T.P., S.M. Adams, J.L. Grimsby, T.L. McGee, D.H. Hong, T. Li, S. Andréasson, and E.L. Berson. 2001. Null RPGRIP1 alleles in patients with Leber

congenital amaurosis. *Am. J. Hum. Genet.* 68:1295–1298. https://doi.org/10.1086/320113

Eblimit, A., T.-M.T. Nguyen, Y. Chen, J. Esteve-Rudd, H. Zhong, S. Letteboer, J. Van Reeuwijk, D.L. Simons, Q. Ding, K.M. Wu, et al. 2015. Spata7 is a retinal ciliopathy gene critical for correct RPGRIP1 localization and protein trafficking in the retina. *Hum. Mol. Genet.* 24:1584–1601. https://doi.org/10.1093/hmg/ddu573

Evans, R.J., N. Schwarz, K. Nagel-Wolfrum, U. Wolfrum, A.J. Hardcastle, and M.E. Cheetham. 2010. The retinitis pigmentosa protein RP2 links pericentriolar vesicle transport between the Golgi and the primary cilium. *Hum. Mol. Genet.* 19:1358–1367. https://doi.org/10.1093/hmg/ddq012

Gerdes, J.M., E.E. Davis, and N. Katsanis. 2009. The vertebrate primary cilium in development, homeostasis, and disease. *Cell.* 137:32–45. https://doi.org/10.1016/j.cell.2009.03.023

Giessl, A., A. Pulvermüller, P. Trojan, J.H. Park, H.-W. Choe, O.P. Ernst, K.P. Hofmann, and U. Wolfrum. 2004. Differential expression and interaction with the visual G-protein transducin of centrin isoforms in mammalian photoreceptor cells. *J. Biol. Chem.* 279:51472–51481. https://doi.org/10.1074/jbc.M406770200

Gilliam, J.C., J.T. Chang, I.M. Sandoval, Y. Zhang, T. Li, S.J. Pittler, W. Chiu, and T.G. Wensel. 2012. Three-dimensional architecture of the rod sensory cilium and its disruption in retinal neurodegeneration. *Cell.* 151:1029–1041. https://doi.org/10.1016/j.cell.2012.10.038

Hidalgo-de-Quintana, J., N. Schwarz, I.P. Meschede, G. Stern-Schneider, M.B. Powner, E.E. Morrison, C.E. Futter, U. Wolfrum, M.E. Cheetham, and J. van der Spuy. 2015. The Leber congenital amaurosis protein AIPL1 and EB proteins co-localize at the photoreceptor cilium. *PLoS One.* 10:e0121440. https://doi.org/10.1371/journal.pone.0121440

Hong, D.-H., B.S. Pawlyk, J. Shang, M.A. Sandberg, E.L. Berson, and T. Li. 2000. A retinitis pigmentosa GTPase regulator (RPGR)-deficient mouse model for X-linked retinitis pigmentosa (RP3). *Proc. Natl. Acad. Sci. USA.* 97:3649–3654. https://doi.org/10.1073/pnas.97.7.3649

Hong, D.-H., G. Yue, M. Adamian, and T. Li. 2001. Retinitis pigmentosa GTPase regulator (RPGRr)-interacting protein is stably associated with the photoreceptor ciliary axoneme and anchors RPGR to the connecting cilium. *J. Biol. Chem.* 276:12091–12099. https://doi.org/10.1074/jbc.M009351200

Jensen, V.L., C. Li, R.V. Bowie, L. Clarke, S. Mohan, O.E. Blacque, and M.R. Leroux. 2015. Formation of the transition zone by Mks5/Rpgrip1L establishes a ciliary zone of exclusion (CIZE) that compartmentalises ciliary signalling proteins and controls PIP2 ciliary abundance. *EMBO J.* 34:2537–2556. https://doi.org/10.15252/embj.201488044

Karlstetter, M., N. Sorusch, A. Caramoy, K. Dannhausen, A. Aslanidis, S. Fauser, M.R. Boesl, K. Nagel-Wolfrum, E.R. Tamm, H. Jägle, et al. 2014. Disruption of the retinitis pigmentosa 28 gene Fam161a in mice affects photoreceptor ciliary structure and leads to progressive retinal degeneration. *Hum. Mol. Genet.* 23:5197–5210. https://doi.org/10.1093/hmg/ddu242

Khanna, H., E.E. Davis, C.A. Murga-Zamalloa, A. Estrada-Cuzcano, I. Lopez, A.I. den Hollander, M.N. Zonneveld, M.I. Othman, N. Waseem, C.F. Chakarova, et al. 2009. A common allele in RPGRIP1L is a modifier of retinal degeneration in ciliopathies. *Nat. Genet.* 41:739–745. https://doi.org/10.1038/ng.366

Kim, D., T.J. Deerinck, Y.M. Sigal, H.P. Babcock, M.H. Ellisman, and X. Zhuang. 2015. Correlative stochastic optical reconstruction microscopy and electron microscopy. *PLoS One.* 10:e0124581. https://doi.org/10.1371/journal.pone.0124581

Kremer, J.R., D.N. Mastronarde, and J.R. McIntosh. 1996. Computer visualization of three-dimensional image data using IMOD. *J. Struct. Biol.* 116:71–76. https://doi.org/10.1006/jsbi.1996.0013

Li, C., V.L. Jensen, K. Park, J. Kennedy, F.R. Garcia-Gonzalo, M. Romani, R. De Mori, A.-L. Bruel, D. Gaillard, B. Doray, et al. 2016. MKS5 and CEP290 Dependent Assembly Pathway of the Ciliary Transition Zone. *PLoS Biol.* 14:e1002416. https://doi.org/10.1371/journal.pbio.1002416

Li, X., M.J. Large, C.J. Creighton, R.B. Lanz, J.-W. Jeong, S.L. Young, B.A. Lessey, W.A. Palomino, S.Y. Tsai, and F.J. Demayo. 2013. COUP-TFII regulates human endometrial stromal genes involved in inflammation. *Mol. Endocrinol.* 27:2041–2054. https://doi.org/10.1210/me.2013-1191

Liu, Q., J. Zuo, and E.A. Pierce. 2004. The retinitis pigmentosa 1 protein is a photoreceptor microtubule-associated protein. *J. Neurosci.* 24:6427–6436. https://doi.org/10.1523/JNEUROSCI.1335-04.2004

Louie, C.M., G. Caridi, V.S. Lopes, F. Brancati, A. Kispert, M.A. Lancaster, A.M. Schlossman, E.A. Otto, M. Leitges, H.-J. Gröne, et al. 2010. AHI1 is required for photoreceptor outer segment development and is a modifier for retinal degeneration in nephronophthisis. *Nat. Genet.* 42:175–180. https://doi.org/10.1038/ng.519

Mastronarde, D.N. 2005. Automated electron microscope tomography using robust prediction of specimen movements. *J. Struct. Biol.* 151:36–51. https://doi.org/10.1016/j.jsb.2005.07.007

May-Simera, H., K. Nagel-Wolfrum, and U. Wolfrum. 2017. Cilia - The sensory antennae in the eye. *Prog. Retin. Eye Res.* 60:144–180. https://doi.org/10.1016/j.preteyeres.2017.05.001

Meindl, A., K. Dry, K. Herrmann, F. Manson, A. Ciccodicola, A. Edgar, M.R.S. Carvalho, H. Achatz, H. Hellebrand, A. Lennon, et al. 1996. A gene (RPGR) with homology to the RCC1 guanine nucleotide exchange factor is mutated in X-linked retinitis pigmentosa (RP3). *Nat. Genet.* 13:35–42. https://doi.org/10.1038/ng0596-35

Mollet, G., F. Silbermann, M. Delous, R. Salomon, C. Antignac, and S. Saunier. 2005. Characterization of the nephrocystin/nephrocystin-4 complex and subcellular localization of nephrocystin-4 to primary cilia and centrosomes. *Hum. Mol. Genet.* 14:645–656. https://doi.org/10.1093/hmg/ddi061

Murga-Zamalloa, C.A., N.J. Desai, F. Hildebrandt, and H. Khanna. 2010. Interaction of ciliary disease protein retinitis pigmentosa GTPase regulator with nephronophthisis-associated proteins in mammalian retinas. *Mol. Vis.* 16:1373–1381.

Otto, E.A., T.W. Hurd, R. Airik, M. Chaki, W. Zhou, C. Stoetzel, S.B. Patil, S. Levy, A.K. Ghosh, C.A. Murga-Zamalloa, et al. 2010. Candidate exome capture identifies mutation of SDCCAG8 as the cause of a retinal-renal ciliopathy. *Nat. Genet.* 42:840–850. https://doi.org/10.1038/ng.662

Patil, H., N. Tserentsoodol, A. Saha, Y. Hao, M. Webb, and P.A. Ferreira. 2012. Selective loss of RPGRIP1-dependent ciliary targeting of NPHP4, RPGR and SDCCAG8 underlies the degeneration of photoreceptor neurons. *Cell Death Dis.* 3:e355. https://doi.org/10.1038/cddis.2012.96

Pazour, G.J., S.A. Baker, J.A. Deane, D.G. Cole, B.L. Dickert, J.L. Rosenbaum, G.B. Witman, and J.C. Besharse. 2002. The intraflagellar transport protein, IFT88, is essential for vertebrate photoreceptor assembly and maintenance. *J. Cell Biol.* 157:103–113. https://doi.org/10.1083/jcb.200107108

Pettersen, E.F., T.D. Goddard, C.C. Huang, G.S. Couch, D.M. Greenblatt, E.C. Meng, and T.E. Ferrin. 2004. UCSF Chimera—a visualization system for exploratory research and analysis. *J. Comput. Chem.* 25:1605–1612.

Rachel, R.A., T. Li, and A. Swaroop. 2012. Photoreceptor sensory cilia and ciliopathies: focus on CEP290, RPGR and their interacting proteins. *Cilia.* 1:22. https://doi.org/10.1186/2046-2530-1-22

Rao, K.N., W. Zhang, L. Li, C. Ronquillo, W. Baehr, and H. Khanna. 2016. Ciliopathy-associated protein CEP290 modifies the severity of retinal degeneration due to loss of RPGR. *Hum. Mol. Genet.* 25:2005–2012. https://doi.org/10.1093/hmg/ddw075

Reiter, J.F., and M.R. Leroux. 2017. Genes and molecular pathways underpinning ciliopathies. *Nat. Rev. Mol. Cell Biol.* 18:533–547. https://doi.org/10.1038/nrm.2017.60

Remans, K., M. Bürger, I.R. Vetter, and A. Wittinghofer. 2014. C2 domains as protein-protein interaction modules in the ciliary transition zone. *Cell Reports.* 8:1–9. https://doi.org/10.1016/j.celrep.2014.05.049

Roepman, R., N. Bernoud-Hubac, D.E. Schick, A. Maugeri, W. Berger, H.H. Ropers, F.P. Cremers, and P.A. Ferreira. 2000. The retinitis pigmentosa GTPase regulator (RPGR) interacts with novel transport-like proteins in the outer segments of rod photoreceptors. *Hum. Mol. Genet.* 9:2095–2105. https://doi.org/10.1093/hmg/9.14.2095

Schaefer, E., A. Zaloszyc, J. Lauer, M. Durand, F. Stutzmann, Y. Perdomo-Trujillo, C. Redin, V. Bennouna Greene, A. Toutain, L. Perrin, et al. 2011. Mutations in SDCCAG8/NPHP10 Cause Bardet-Biedl Syndrome and Are Associated with Penetrant Renal Disease and Absent Polydactyly. *Mol. Syndromol.* 1:273–281. https://doi.org/10.1159/000331268

Shu, X., A.M. Fry, B. Tulloch, F.D.C. Manson, J.W. Crabb, H. Khanna, A.J. Faragher, A. Lennon, S. He, P. Trojan, et al. 2005. RPGR ORF15 isoform co-localizes with RPGRIP1 at centrioles and basal bodies and interacts with nucleophosmin. *Hum. Mol. Genet.* 14:1183–1197. https://doi.org/10.1093/hmg/ddi129

Sigal, Y.M., C.M. Speer, H.P. Babcock, and X. Zhuang. 2015. Mapping Synaptic Input Fields of Neurons with Super-Resolution Imaging. *Cell.* 163:493–505. https://doi.org/10.1016/j.cell.2015.08.033

Thompson, R.E., D.R. Larson, and W.W. Webb. 2002. Precise Nanometer Localization Analysis for Individual Fluorescent Probes. *Biophys. J.* 82:2775–2783. https://doi.org/10.1016/S0006-3495(02)75618-X

Wang, H., A.I. den Hollander, Y. Moayedi, A. Abulimiti, Y. Li, R.W.J. Collin, C.B. Hoyng, I. Lopez, E.B. Abboud, A.A. Al-Rajhi, et al. 2009. Mutations in SPATA7 cause Leber congenital amaurosis and juvenile retinitis pigmentosa. *Am. J. Hum. Genet.* 84:380–387. https://doi.org/10.1016/j.ajhg.2009.02.005

Wensel, T.G., Z. Zhang, I.A. Anastassov, J.C. Gilliam, F. He, M.F. Schmid, and M.A. Robichaux. 2016. Structural and molecular bases of rod photoreceptor morphogenesis and disease. *Prog. Retin. Eye Res.* 55:32–51. https://doi.org/10.1016/j.preteyeres.2016.06.002

Wheway, G., M. Schmidts, D.A. Mans, K. Szymanska, T.T. Nguyen, H. Racher, I.G. Phelps, G. Toedt, J. Kennedy, K.A. Wunderlich, et al. University of Washington Center for Mendelian Genomics. 2015. An siRNA-based functional genomics screen for the identification of regulators of ciliogenesis and ciliopathy genes. *Nat. Cell Biol.* 17:1074–1087. https://doi.org/10.1038/ncb3201

Williams, C.L., C. Li, K. Kida, P.N. Inglis, S. Mohan, L. Semenec, N.J. Bialas, R.M. Stupay, N. Chen, O.E. Blacque, et al. 2011. MKS and NPHP modules cooperate to establish basal body/transition zone membrane associations and ciliary gate function during ciliogenesis. *J. Cell Biol.* 192:1023–1041. https://doi.org/10.1083/jcb.201012116

Zhao, Y., D.-H. Hong, B. Pawlyk, G. Yue, M. Adamian, M. Grynberg, A. Godzik, and T. Li. 2003. The retinitis pigmentosa GTPase regulator (RPGR)-interacting protein: subserving RPGR function and participating in disk morphogenesis. *Proc. Natl. Acad. Sci. USA.* 100:3965–3970. https://doi.org/10.1073/pnas.0637349100